The Role of Entrainment in the Diurnal Cycle of Continental Convection

ANTHONY D. DEL GENIO

NASA Goddard Institute for Space Studies, New York, New York

JINGBO WU

Department of Applied Physics and Applied Mathematics, Columbia University, New York, New York

(Manuscript received 9 July 2009, in final form 16 December 2009)

ABSTRACT

In continental convective environments, general circulation models typically produce a diurnal cycle of rainfall that peaks close to the noon maximum of insolation, hours earlier than the observed peak. One possible reason is insufficient sensitivity of their cumulus parameterizations to the state of the environment due to weak entrainment. The Weather Research and Forecasting (WRF) model, run at cloud-resolving (600 and 125 m) resolution, is used to study the diurnal transition from shallow to deep convection during the monsoon break period of the Tropical Warm Pool–International Cloud Experiment. The WRF model develops a transition from shallow to deep convection in isolated events by 1430–1500 local time. The inferred entrainment rate weakens with increasing time of day as convection deepens. Several current cumulus parameterizations are tested for their ability to reproduce the WRF behavior. The Gregory parameterization, in which entrainment rate varies directly with parcel buoyancy and inversely as the square of the updraft speed, is the best predictor of the inferred WRF entrainment profiles. The Gregory scheme depends on a free parameter that represents the fraction of buoyant turbulent kinetic energy generation on the cloud scale that is consumed by the turbulent entrainment process at smaller scales. A single vertical profile of this free parameter, increasing with height above the boundary layer but constant with varying convection depth, produces entrainment rate profiles consistent with those inferred from the WRF over the buoyant depth of the convection. Parameterizations in which entrainment varies inversely with altitude or updraft speed or increases with decreasing tropospheric relative humidity do not perform as well. Entrainment rate at cloud base decreases as convection depth increases; this behavior appears to be related to an increase in vertical velocity at downdraft cold pool edges.

1. Introduction

A consistent feature of summer continental climates is the tendency for rainfall to peak in middle to late afternoon, or in some places in the evening, many hours after the noon peak in insolation (Nesbitt and Zipser 2003; Dai 2006; Yang and Smith 2006; Hirose et al. 2008). In some cases this may be controlled by large-scale dynamics or orography (Wallace 1975), but in many situations of isolated surface-driven convection an environment containing convective available potential energy for deep ascent by noon nonetheless exhibits only shallow convection until hours later. It has been suggested that the transition occurs when shallow clouds on average become unstable to deeper ascent (C.-M. Wu et al. 2009).

General circulation models (GCMs), on the other hand, tend to produce peak rainfall near the time of the noon peak in insolation (Guichard et al. 2004). This is true of both climate models (Dai 2006) and numerical weather prediction models (Betts and Jakob 2002; Janowiak et al. 2007). This has important practical ramifications, as errors in the diurnal cycle of convection produce an erroneous surface water balance and an overestimate of shortwave cloud forcing.

A likely candidate for the diurnal cycle problem in GCMs is the turbulent entrainment of environmental air assumed by the models' cumulus parameterizations. Large-eddy simulation (LES) models have been used to show that implied entrainment rates in shallow convection are considerably larger than typical values assumed in GCMs (Siebesma and Cuijpers 1995). Derbyshire et al.

Corresponding author address: Anthony D. Del Genio, NASA Goddard Institute for Space Studies, 2880 Broadway, New York, NY 10025.
E-mail: adelgenio@giss.nasa.gov

DOI: 10.1175/2009JCLI3340.1

(2004) showed that cloud-resolving models (CRMs) were sensitive to the presence of dry air in the free troposphere, producing a transition from shallow to deep convection as the troposphere moistened (see also Redelsperger et al. 2002), while single-column model (SCM) versions of several GCMs did not, presumably because their entrainment rates were too weak. Grabowski et al. (2006) suggested that entrainment rate, which is often constant or a fixed function of altitude in GCMs, must decrease over the course of the day in order for the diurnal cycle to be portrayed accurately. Kuang and Bretherton (2006) and Khairoutdinov and Randall (2006) have in fact shown using different CRM simulations, one for tropical ocean and the other tropical land convection, that entrainment rates are weaker for deep convection than for shallow convection. They suggested that this is due to the formation of downdraft-driven cold pools. Cold pool convergence creates larger eddies at the gust front in both models; these eddies entrain less and give rise to deeper convection than the smaller turbulent boundary layer eddies that produce shallow cumulus.

Early GCMs included a specification for at least part of the cumulus mass flux to go into undilute plumes that, given the mean thermodynamic properties of the boundary layer, would produce maximum convective cloud tops similar to those observed. It eventually became clear, though, that setting a minimum nonzero entrainment rate was beneficial to the simulation of dynamical phenomena such as the Madden–Julian oscillation (Tokioka et al. 1988). Lin and Arakawa (1997) showed that, in a 2D CRM, entrainment was strong near the boundary layer and weaker above, and several models have adopted an inverse-height relationship for entrainment rate (Jakob and Siebesma 2003; Zhang 2009). More recently, Khairoutdinov and Randall (2006) found that, in a high-resolution 3D simulation, undilute plumes were completely absent. GCMs have nonetheless not yet truly confronted the need for their convective clouds to entrain interactively and more strongly, although one model now directly relates the entrainment rate of deep convection to the subsaturation of the troposphere (Bechtold et al. 2008). Rio et al. (2009) use a different approach, employing separate shallow and deep convection schemes in a single-column model to produce a realistic mid-afternoon shallow–deep convection transition. The question remains open, though, as to what physics controls entrainment rate and whether a single convection scheme with thermodynamic state-dependent entrainment can simulate a realistic convection diurnal cycle.

Our goal in this paper is to use a CRM to simulate the diurnal transition of continental convection from shallow to deep and to infer the entrainment rates for convection of varying depths. The model and simulation setup are discussed in section 2 and the results shown in section 3. These results are used to evaluate several candidate entrainment parameterizations in section 4 and to explore the role of downdraft cold pools in section 5. Section 6 discusses the ramifications of the present work for future parameterization development.

2. Simulations

a. WRF model

The Weather Research and Forecasting (WRF) mesoscale numerical weather prediction model with the Advanced Research WRF dynamical solver, version 2.2 (Skamarock et al. 2007) is used to simulate Tropical Warm Pool–International Cloud Experiment (TWP–ICE) convection. The model has fully compressible nonhydrostatic equations and complete Coriolis and curvature terms. The vertical coordinate is mass-based and terrain following. The model uses Arakawa C-grid staggering. The prognostic variables are in scalar-conserving flux form.

The simulations described in this paper resolve moist convection (see section 2b), so no cumulus parameterization is utilized. Microphysics is treated with the Thompson scheme (Thompson et al. 2004), which has six classes of hydrometeors including water vapor, cloud liquid, rain, cloud ice, snow, and graupel and is designed to limit excessive snow and graupel growth. Planetary boundary layer (PBL) turbulence on scales smaller than those resolved is treated with the Yonsei University scheme (YSU) (Hong and Pan 1996; Skamarock et al. 2007), which uses a countergradient flux approach for nonlocal effects and the Monin–Obukhov surface scheme. All runs employ a thermal diffusion land surface scheme, with fixed soil moisture that depends on land use and season (Skamarock et al. 2007). Radiation is treated with the Rapid Radiative Transfer Model (RRTM) longwave scheme, a spectral-band radiative transfer model using the correlated-k method (Mlawer et al. 1997), and the Dudhia (1989) shortwave scheme.

b. Simulation setup

Our simulations are based loosely on the monsoon break period of the 2006 TWP–ICE in the area near Darwin, Australia (May et al. 2008). TWP–ICE included a large-scale array of six sounding stations from which mean thermodynamic profiles and advective forcing products were derived (Xie et al. 2010). The runs we conduct are specified in Table 1. The CONTROL simulation is identical to the ''Thompson-fine'' simulation of J. Wu et al. (2009), with 600-m horizontal resolution and 50 vertical layers. The model domain is approximately 280 km × 280 km (11.0°–13.5°S, 129.5°–132.0°E, equivalent to the inner domain shown in Fig. 1 of J. Wu et al.

TABLE 1. Description of WRF simulations.

Simulation name	Horizontal resolution (m)	Number of layers	Domain size (km)	Humidity profile
CONTROL	600	50	280 × 280	Observed
FINE	125	145	75 × 75	Observed
RH90	600	50	280 × 280	Relaxed toward 90% 250–700 mb

2009). It is comparable in location and size to the array from which the TWP–ICE forcing products were derived. The model is run with a 2.5-s time step and sampled every 5 min, and results shown in this paper correspond to approximately a 120 km × 120 km subdomain that contains most of the simulated convection. As described by J. Wu et al. (2009), the WRF model is driven by 6-hourly European Centre for Medium-Range Weather Forecasts (ECMWF) winds at the boundaries, and temperature and humidity profiles are updated at the boundaries every 6 h to match the TWP–ICE forcing products.

The WRF model gives realistic statistics of convection depth and strength over this period, with CAPE close to that observed and stronger updrafts than at other times (J. Wu et al. 2009). During the break period, high pressure to the south produces weak easterlies over the TWP–ICE domain, and convection is generated by strong local surface sensible and latent heat fluxes rather than being controlled synoptically, as it is during active monsoon phases (May et al. 2008). TWP–ICE included only two inland sounding sites and three surface flux measurement stations; the flux stations were fairly close to the coast and experienced periodic outages during the experiment, so actual conditions inland are not well constrained observationally. The lack of large-scale control, the uncertainties in inland thermodynamic structure, and the effect of the WRF fixed soil moisture assumption on surface fluxes mean that it is not feasible to simulate individual instantaneous convective events on any given day. Rather, we choose to analyze a transition from shallow to deep convection in the WRF on 10 February 2006 that captures features of the observed climatological continental diurnal cycle near Darwin during monsoon break periods. The CONTROL simulation is initiated at 2130 LT the previous evening, ~15 h before the onset of convection.

Although 600-m resolution is considered high enough to explicitly simulate many aspects of deep convection, this is not true of shallow convection, and several studies in fact indicate that the character of deep convection changes at resolutions of 100–200 m (Petch et al. 2002; Bryan et al. 2003). Bryan et al. argue that only at fine resolution do simulations resolve an inertial subrange and produce circulations that are themselves turbulent. This is expected to be of special relevance for questions of entrainment. Unfortunately, computational limitations preclude performing a simulation at this horizontal resolution (and comparable vertical resolution) over the domain size on which the TWP–ICE forcing products are calculated. Instead, we conducted a fine-resolution simulation at 125-m horizontal resolution and with 145 vertical layers (ranging from ~75 m thickness in the PBL to ~490 m at the 50-mb top in the stratosphere) over a ~75 km × 75 km mostly inland domain (12.4°–13.1°S, 130.4°–131.1°E) for comparison with the CONTROL results over the larger domain. Over the small FINE domain, the sampling of convection (especially deep) is sparser and the results therefore noisier than those of CONTROL. However, the statistics are good enough to illustrate similarities and differences associated with resolution changes. This run was initiated at 0330 LT and uses a 1.5-s time step until convection onset at 1230 LT and a 1-s time step thereafter.

Figure 1 shows undilute parcel buoyancy and environmental relative humidity (RH) profiles at different times of day for CONTROL and FINE. The near-surface boundary layer is fairly dry during the break period, and thus the level of free convection is not reached until parcels rise to ~2-km altitude. Above this altitude, though, the most unstable undilute parcels become strongly buoyant up to 13–14-km altitude as early as 1200 LT. This is due to surface latent heat and sensible heat fluxes that peak shortly after noon, associated with a surface temperature that does the same (Fig. 2). Thus, if the shallow–deep transition is to occur later in the afternoon, it must be due to entrainment. The RH profiles show a sufficiently dry (~70%) free troposphere between 2- and 8-km altitude for entrainment to be a significant factor in parcel buoyancy. The FINE thermodynamic structure is slightly more unstable and drier than that for CONTROL because its domain is more continental but has similar features.

Finally, since one of the questions about the shallow–deep transition is whether tropospheric RH influences convection depth indirectly via the thermodynamic properties of entrained air, or directly by affecting the entrainment rate itself, we also conducted a simulation RH90 that is identical to CONTROL except that we restore the RH profile at the domain boundaries every 6 h to 90% between 250 and 700 mb. This produces a time mean RH profile (not shown) that increases with

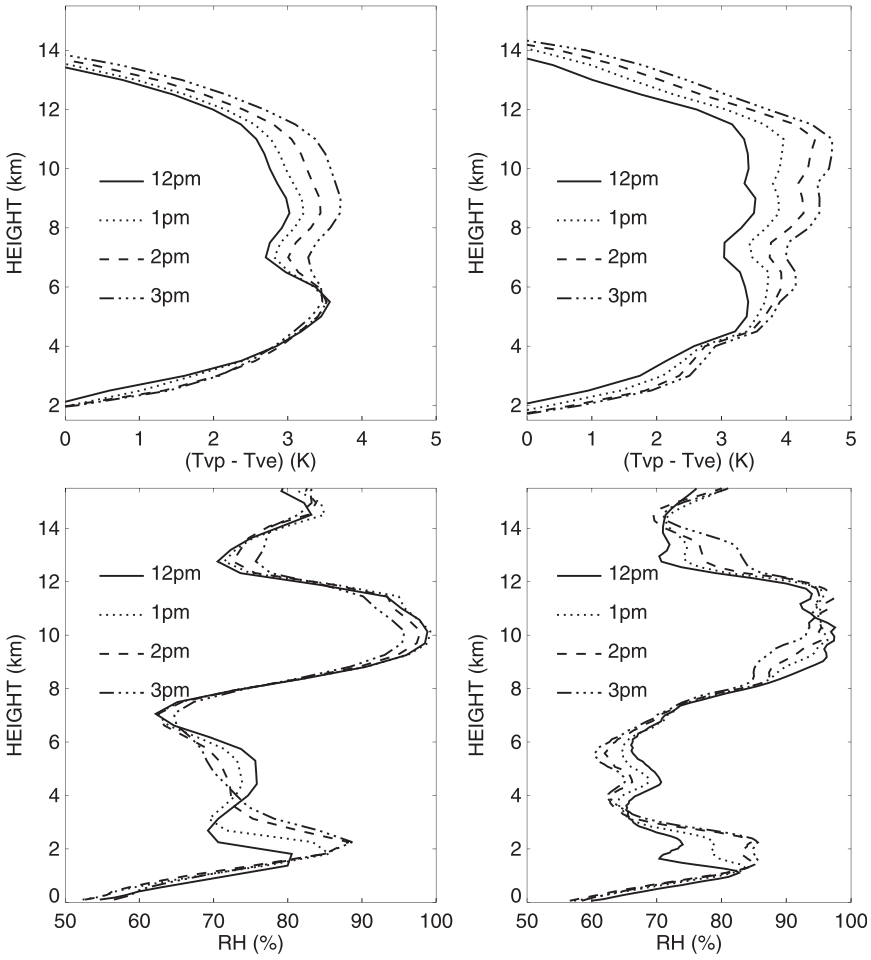

FIG. 1. (top) Undilute parcel buoyancy profiles for the (left) CONTROL and (right) FINE simulations, based on the parcel with the highest equivalent potential temperature in the lowest 3 km. (bottom) As in (top), but environmental relative humidity profiles.

height in the midtroposphere and is >80% everywhere there, as opposed to the CONTROL profile that generally decreases with height in midtroposphere.

3. Diurnal cycle of convection and entrainment

The bottom panel of Fig. 2 shows that, despite the near-noon peaks of surface heat fluxes and temperature, precipitation lags by many hours. Figure 3 shows the corresponding mean WRF convective updraft/downdraft speed and precipitating condensate profiles as a function of time for the CONTROL simulation. Moist convective updraft columns are defined as multiple contiguous buoyant layers with bases below the 750-mb level, vertical velocity >0, total hydrometeor mixing ratio $\geq$0.1 g kg^{-1}, and cloud condensate mixing ratio $>10^{-3}$ g kg^{-1}. Convective downdraft columns are defined as contiguous layers with vertical velocity <0 that begin below the maximum height of updrafts at that time, penetrate below the 1.5-km level, and satisfy the total hydrometeor and cloud condensate criteria at their initiation level. Above the level of neutral buoyancy we continue the updraft until either the vertical velocity decreases to 0.1 m s^{-1} or the cloud condensate criterion is not satisfied. Convective clouds begin to appear shortly after noon, but they are shallow despite the deep unstable layer seen in Fig. 1. The clouds gradually deepen over the next two hours as the shallow cumulus clouds moisten the atmosphere from 2 to 4 km (Fig. 1). By 1330–1400 LT cloud tops have reached the congestus stage with tops at ~600 mb, downdrafts have strengthened, and precipitation has started to reach the ground. Within the next hour the transition to deep convection takes place. The convection has penetrated to the tropopause by 1530–1600 LT, at which time surface precipitation reaches its maximum value. This is consistent with the observed

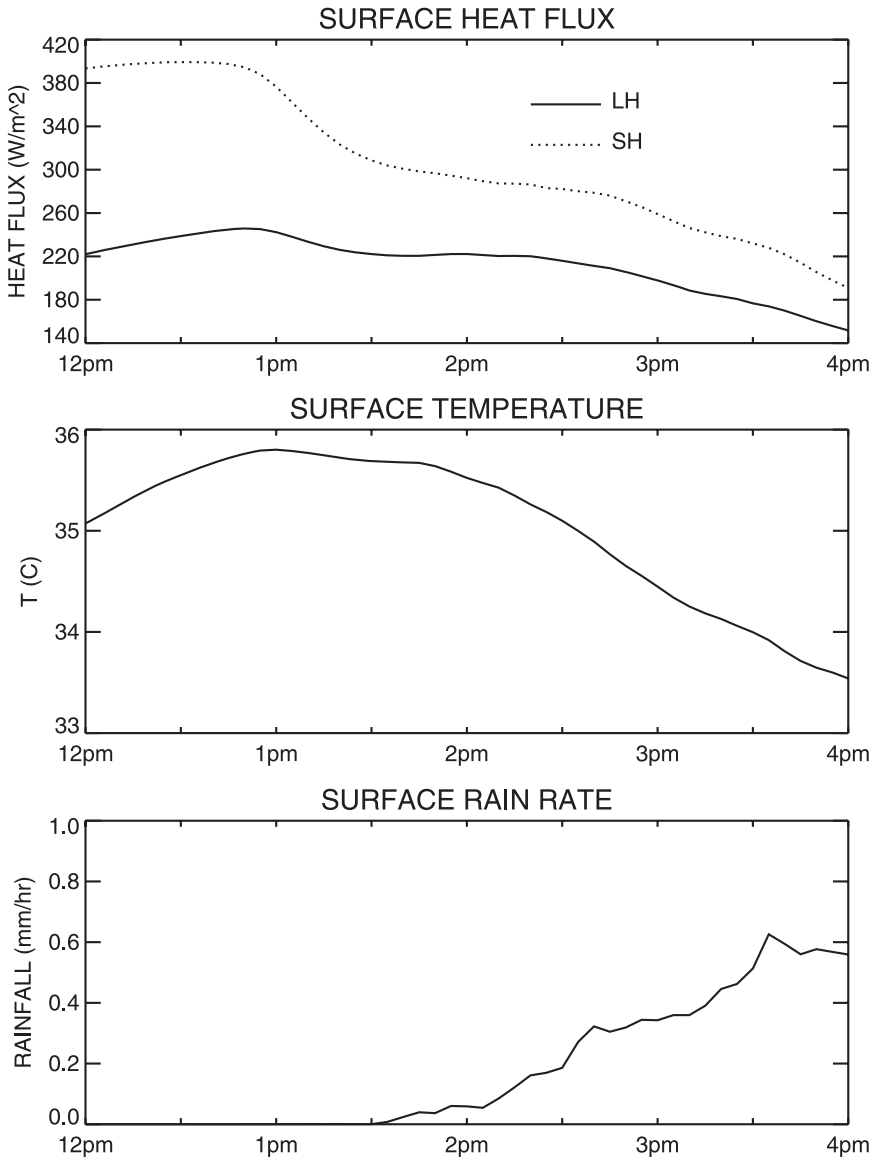

FIG. 2. Diurnal variation of (top) surface sensible and latent heat fluxes, (middle) surface temperature, and (bottom) precipitation averaged over land grid boxes in CONTROL.

time of the rainfall peak at Darwin during monsoon break periods (Rauniyar and Walsh 2009). The FINE simulation (not shown) begins convecting about a half hour later than CONTROL but still develops deep convection by ~1500 LT; its downdrafts are ~1 m s^{-1} stronger than those in CONTROL.

Figure 4 shows the CONTROL transition viewed in a complementary fashion, with cloud masks at 701, 507, and 300 mb overlain on maps of near-surface temperature for different times of day. The coastline is clearly visible as the sharp transition from red to blue in the surface temperature field early in the day. By 1430 LT, cold pools of eventual width 10–20 km with temperature depressions of ~2°–4°C begin to appear over land, the largest of them in the locations that develop deep convection. There is a general tendency for convective clouds to develop near the gust front at the edges of the cold pools, a behavior also seen in the simulation of Khairoutdinov and Randall (2006). Note that while some of the clouds at 507 mb are merely in the midst of the transition to deep convection, others are true congestus that do not develop further. Figure 5 shows the large-scale vertical velocity field over the domain as a function of time. Large-scale ascent is restricted to the boundary layer and from 8 to 12 km during the first part of the afternoon; the lower–midtroposphere actually

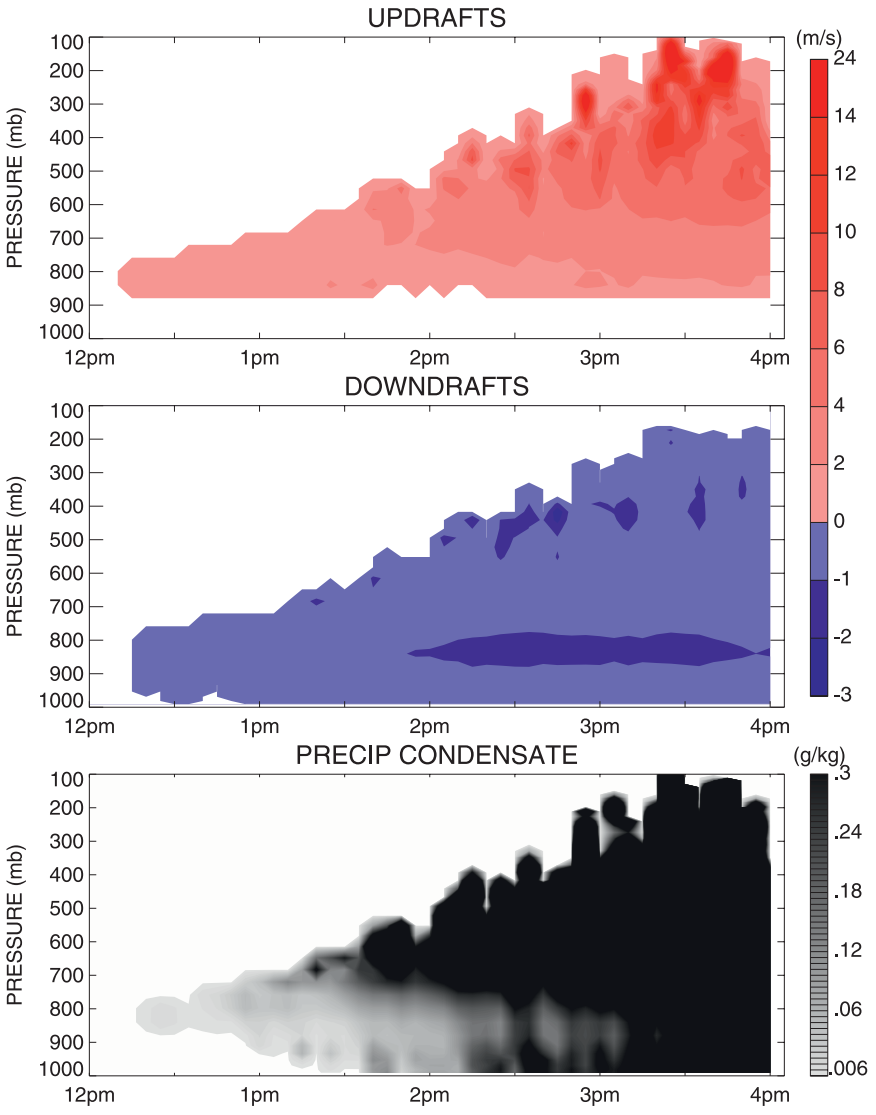

FIG. 3. Mean (top) updraft speed, (middle) downdraft speed, and (bottom) precipitating condensate mixing ratio, averaged over all convective columns, for the CONTROL simulation.

experiences large-scale subsidence that strengthens for the first few hours of the afternoon. Thus, the convection in our simulations deepens *despite* unfavorable large-scale forcing rather than because of favorable large-scale conditions. Ascent through most of the troposphere sets in and strengthens after 1500 LT, but this is a response to the convection that already exists rather than a cause of it.

Figure 6 shows actual buoyancy and convective updraft speed profiles for grid cells of different convection depths for the CONTROL and FINE runs. In CONTROL buoyancy generally increases with convection depth, and deep events start out at cloud base with slightly higher buoyancies than shallow events. In FINE buoyancies are more similar near cloud base and are slightly smaller overall. The deepest events are actually less buoyant than the shallower events, although this may be a result of the small number of samples of deep convection in this simulation. Updraft speeds in CONTROL become stronger at all levels as convection deepens; for FINE the updraft speeds of the deeper events are slightly weaker, consistent with the smaller buoyancies, and speeds of events of different depth begin to diverge from each other only as the shallower events begin to lose buoyancy.

Following Kuang and Bretherton (2006) we define the frozen moist static energy (MSE) as $h = c_pT + gz + Lq_v - L_fq_i$, where c_p is the specific heat at constant pressure, T is temperature, g is gravity, z is height, L is the latent

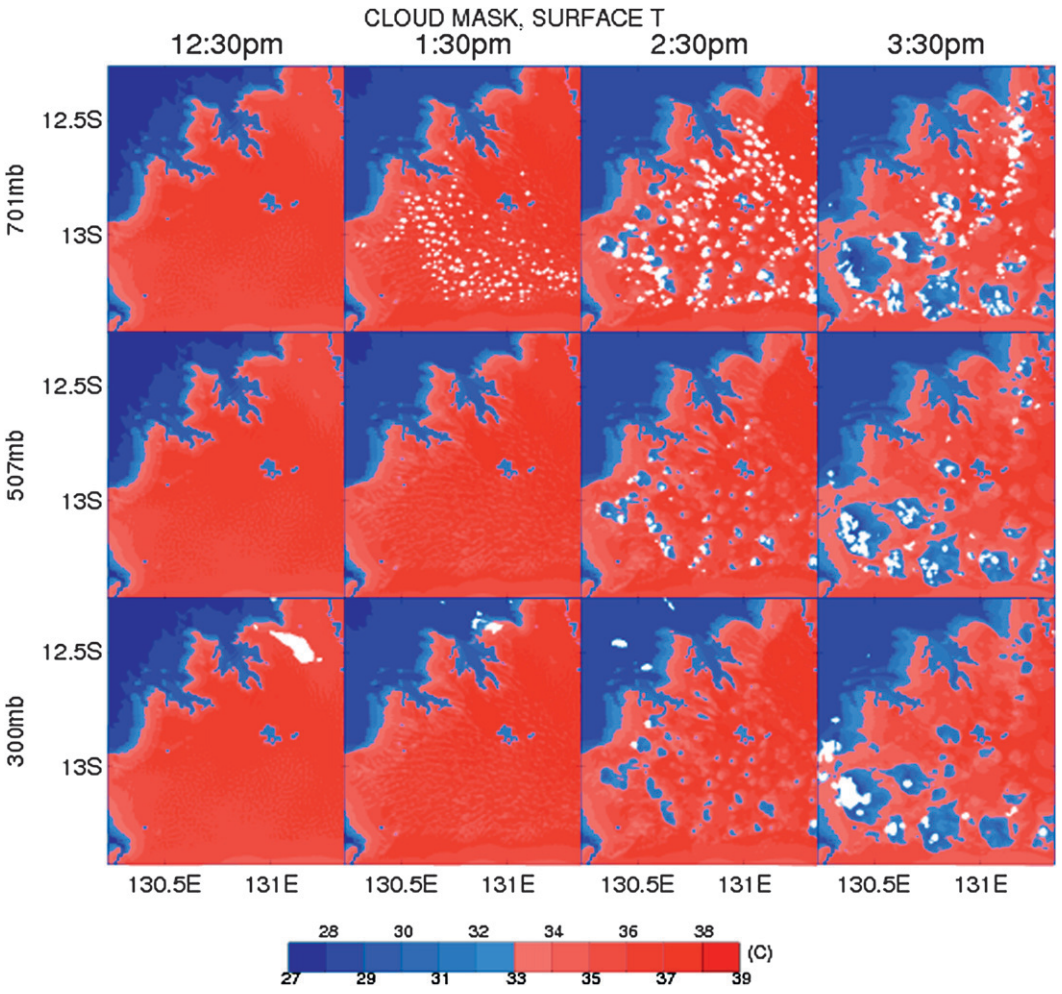

FIG. 4. Near-surface temperature, with cloud mask overlain in white, at (top) 701, (middle) 507, and (bottom) 300 mb at different times of day in the CONTROL simulation.

heat of condensation, q_v is the water vapor mixing ratio, L_f is the latent heat of freezing, and q_i is the cloud ice mixing ratio. MSE is conserved for moist adiabatic ascent of convective parcels even in the presence of liquid precipitation or evaporation. Thus, below levels at which ice precipitation forms, MSE remains constant unless it is diluted by entrainment mixing with the large-scale environment. We can therefore write

$$\frac{dh_u}{dz} = \varepsilon(h_e - h_u), \tag{1}$$

where the subscripts u and e indicate the MSE for the convective updraft and the environment, respectively, and ε is the entrainment rate, that is, the fractional rate at which mass is added to the updraft per kilometer of rise. We calculate dh_u/dz for each convective column, and then using the domain mean MSE for h_e and (1) we can infer the entrainment rate. (Using the mean MSE outside clouds for h_e has less than a 2% effect.) The result should be interpreted as an "effective" entrainment rate appropriate for comparison to a GCM cumulus parameterization because the actual entrained air close to the cloud edge may have a somewhat different MSE than the domain mean value.

Our calculation assumes that the convective columns are upright; that is, we do not use complex parcel trajectory methods (e.g., Lin and Arakawa 1997) to follow convective elements as they rise from the boundary layer. This assumption may have more of an effect in the FINE simulation than in CONTROL. Shear-induced tilt of convective columns is limited during this time period; there is a weak eastward jet just above cloud base and at higher levels shear is $\sim$1 m s^{-1} km^{-1} and of changing sign with height. Furthermore, we restrict our analysis to pressures $>$400 mb, a level above which results become

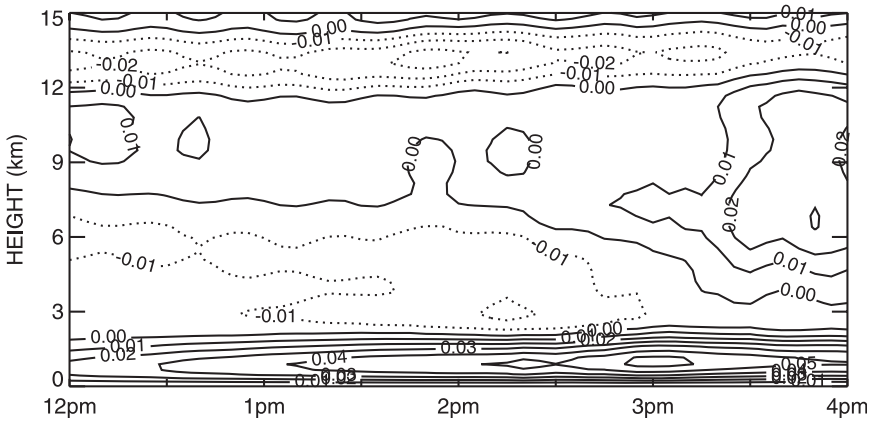

FIG. 5. Height vs time evolution of domain mean large-scale vertical velocity. Solid contours represent upward motion and dashed contours downward motion.

ambiguous as the parcel–environment difference becomes small and ice precipitation causes MSE not to be conserved. Finally, for most of our calculations we only consider cloudy buoyant updrafts, so if a convective cell tilts our calculation terminates once we encounter clear or nonbuoyant air. To estimate the effect of tilt, we manually determined the actual h_u profile in several subsets of convective cells in the CONTROL run, using the horizontal position of the peak updraft speed at each level to define the cell while accounting for any tilt. The resulting mean entrainment rate for deep cells that penetrate to the 300–400-mb level near 1530 LT is 17% smaller than our estimate for assumed upright cells. For shallow cells near 1330 LT the difference is 10%.

Figure 7 (left) shows the mass-flux weighted mean inferred entrainment rate profiles for CONTROL at different times of day, including all updrafts, whether or not they are cloudy or buoyant. The weighting is based on our objective of determining an entrainment rate that is appropriate for a mass-flux cumulus parameterization. Below cloud base entrainment rate decreases with height with approximately the inverse-z dependence assumed in some studies. However, above cloud base the entrainment rate increases and then becomes almost constant with height rather than decreasing further. When we restrict the calculation to only cloudy buoyant updrafts (Fig. 7, right), there is no sign of inverse-z dependence because of the high altitude of cloud base. Entrainment rate monotonically decreases with increasing time of day, as suggested by Grabowski et al. (2006), with typical midtroposphere values of $\varepsilon \sim 0.5$–1.0 km^{-1}, much higher than assumed by most cumulus parameterizations at these levels.

As seen from Fig. 4, the entrainment rate at any time of day is a mixture of contributions from convection of different depths. Figure 8 stratifies the entrainment rate profiles by convection top pressure instead, for both the CONTROL and FINE simulations; these profiles are similar to what a cumulus parameterization with a spectrum of cloud-top heights should produce in this environment, although each curve may mix some clouds that are still rising with those that have detrained at the indicated level. The deepest convective events have the weakest entrainment, ~0.2 km^{-1} in CONTROL and somewhat larger and increasing with height in FINE, consistent with the likely more turbulent nature of the higher-resolution run. In both runs entrainment weakens with increasing convection depth.

4. Parameterization tests

Although many GCMs use fixed prescriptions for entrainment, several parameterizations of entrainment rate as functions of the atmospheric state have been proposed. Our WRF simulations can be used to evaluate these schemes.

Gregory (2001) proposes a diagnostic equation for the convective updraft speed w_c given by

$$\frac{1}{2}\frac{\partial w_c^2}{\partial z} = ag\left(\frac{T_v'}{\overline{T_v}} - q_h\right) - \varepsilon(z)w_c^2 - bD(z)w_c^2, \qquad (2)$$

where g is gravity, T_v is virtual temperature, the prime and overbar are in-cloud and environmental values, q_h is hydrometeor mixing ratio, $D(z)$ is the fractional detrainment rate due to cloud outflow, and $\varepsilon(z)$ is the fractional entrainment rate. The free parameter a is related to the virtual mass coefficient used by Simpson and Wiggert (1969) and interpreted by Gregory as accounting for the retarding effect of the growth of turbulence as the parcel ascends, and b is a free parameter used to treat deceleration by cumulus pressure gradient forces

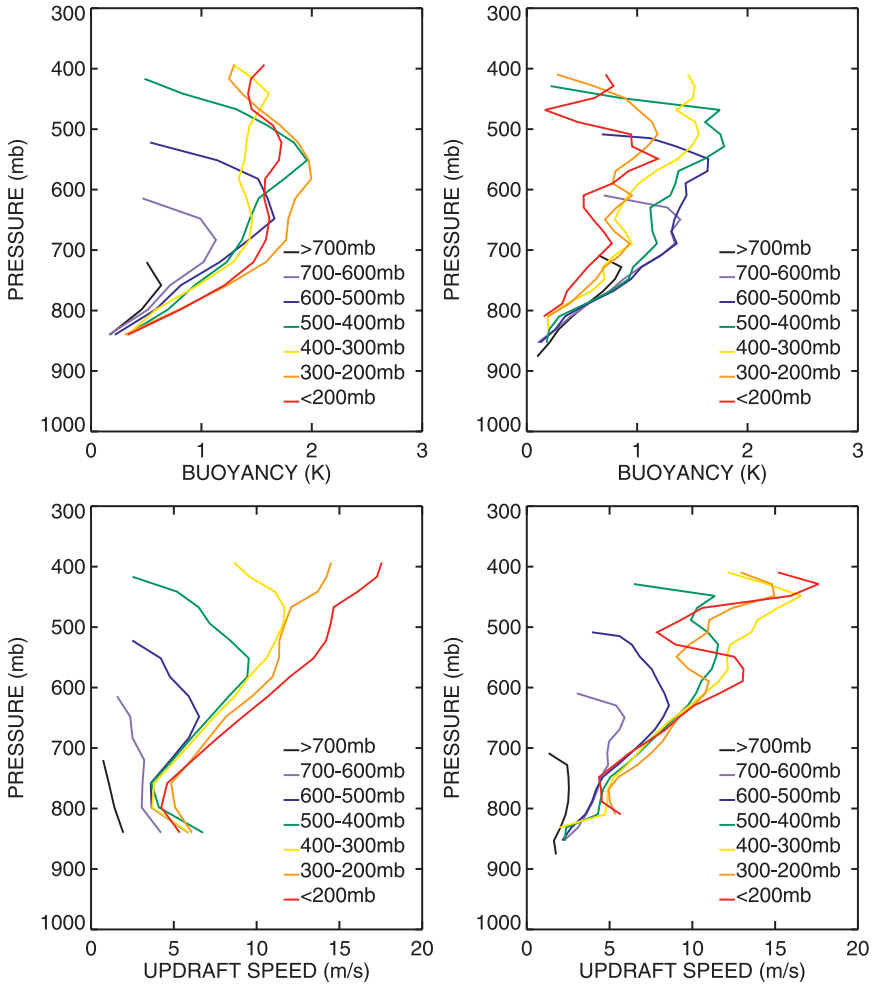

FIG. 6. Vertical profiles of (top) parcel buoyancy and (bottom) updraft speed averaged over all convective columns with tops in various pressure intervals in (left) CONTROL and (right) FINE.

in terms of the detrainment. Entrainment is assumed to reduce parcel buoyancy by a constant factor C:

$$\varepsilon(z)w_c^2 = C'ag\left(\frac{T_v'}{\overline{T}_v} - q_h\right) = C'aB = CB, \qquad (3)$$

where B is the parcel buoyancy. Gregory assumes $a = 1/6$ and takes $C' = 0.5$ for shallow convection and 0.25 for deep convection. This formulation is motivated by a buoyant turbulence scaling for shallow cumulus proposed by Grant and Brown (1999) on the basis of LES experiments. The basic argument is energetic rather than thermodynamic: Entrained air must be accelerated to the convective updraft speed, and C simply represents the fraction of the buoyant turbulent kinetic energy production that is available for entrainment. In this view, the energy-generating cloud scales produce entrainment at smaller scales through the inertial cascade, and thus entrainment is a reflection of the dissipation process, which limits updraft speeds. This scheme has recently been tested in a GCM by Chikira (2008).

From (3), $C = \varepsilon w_c^2/B$. All quantities on the right-hand side can be calculated from the WRF simulations (Figs. 6 and 8), so it is possible to test Gregory's parameterization by determining whether the implied value of C is really a constant. The results are shown in Fig. 9 for the CONTROL and FINE simulations. Here C varies with height, decreasing just above cloud base and then increasing above the 700-mb level. There is also some scatter near cloud base, where B is very small, and in the upper troposphere, where sampling errors increase and C unrealistically begins to exceed 1; the poorer sampling in FINE also creates a noisier result. Overall, though, the implied vertical profiles of C for different convection depths are impressively similar to each other, considering the substantial differences among convection types

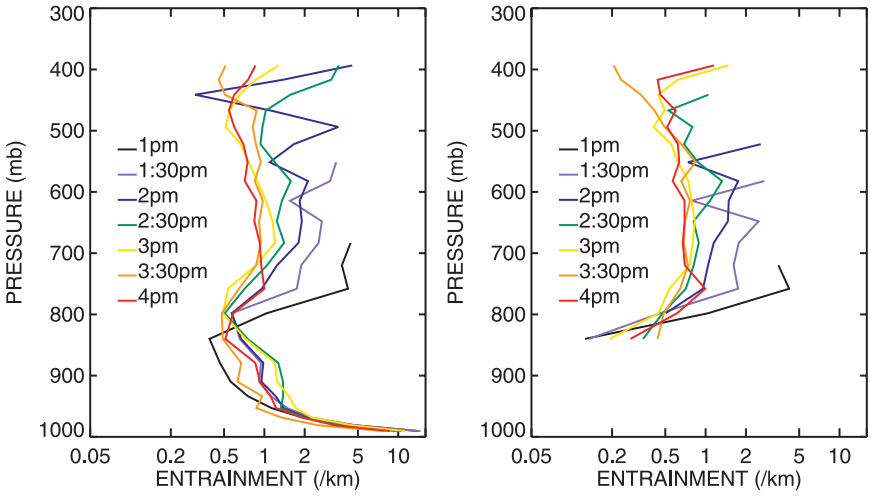

FIG. 7. Mass-flux weighted mean entrainment rate profiles at different times of day for convective columns in the CONTROL simulation, (left) including all levels with positive vertical velocity and (right) including only levels that are also cloudy and buoyant. The 0°C level is at 555 mb.

in the individual values of ε, w_c, and B. We calculated C from the mean values of ε, w_c, and B over all convective cells, as would be appropriate for comparison to a cumulus parameterization. An almost identical profile results if C is calculated individually for each convective column and the resulting values of C averaged; however, there is considerable variation in C from one cell to another (standard deviation approximately 0.4–0.7).

It is possible that the entrainment and implied C profiles are specific to the thermodynamic structure during the TWP–ICE break period. The RH90 simulation provides one test of this. As seen in Fig. 10, the small buoyancies and large boundary layer entrainment of drier air early in the day limit convection depth in early afternoon despite the humid conditions above. The effect of the humid free troposphere is instead felt as an earlier (~1 h) transition to deep convection and similarly earlier time of peak precipitation relative to CONTROL. Downdrafts are also slightly weaker in this run. Figure 11 shows the ε and C profiles for the RH90 simulation. Entrainment rates near cloud base are more similar for different convection depths in this simulation, but the overall vertical structure of ε is similar to that in CONTROL and FINE, suggesting that entrainment rate does not

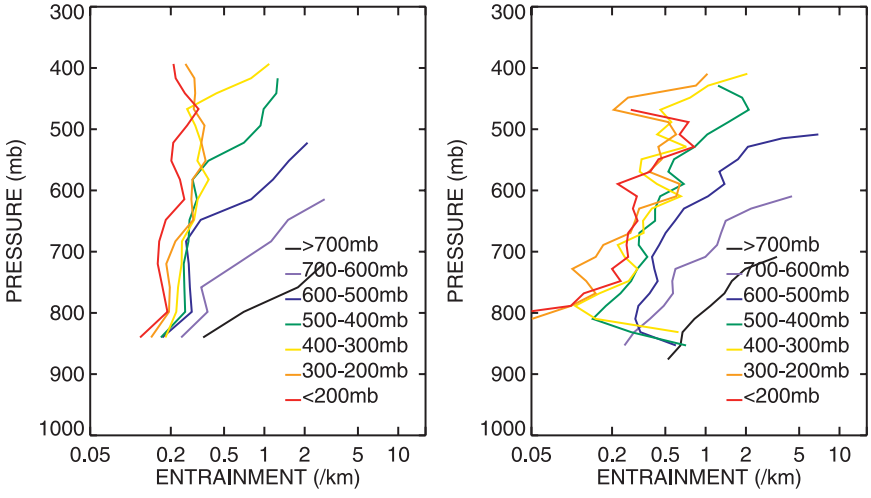

FIG. 8. Mass-flux weighted mean entrainment rate profiles for cloudy buoyant convective columns sorted according to events with tops in different pressure ranges for (left) CONTROL and (right) FINE.

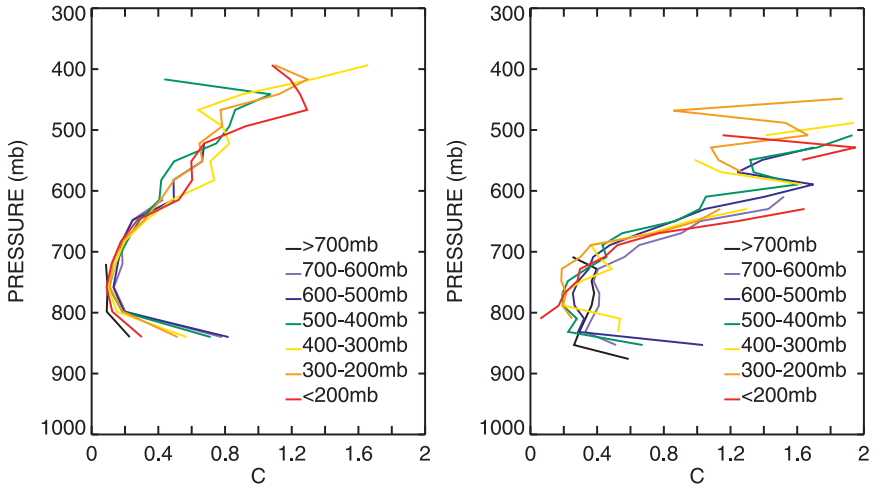

FIG. 9. Inferred mean vertical profiles of the Gregory (2001) free parameter C for (left) CONTROL and (right) FINE.

explicitly depend on RH. Furthermore, the implied C profiles are once again similar for different convection depths and similar to those in the other two runs. We therefore conclude that the Gregory (2001) entrainment parameterization is a viable option for GCMs, regardless of the thermodynamic conditions, if the vertical profile of C can be determined.

An alternative entrainment rate parameterization has been proposed by Neggers et al. (2002). Neggers et al. performed LES simulations of several shallow cumulus field experiment case studies and showed that, at the parcel scale, the model cloud vertical structure and updraft speed profile were very well approximated using an entrainment rate given by

$$\varepsilon(z) = \frac{\eta}{\tau}\frac{1}{w_c}, \tag{4}$$

where τ is an eddy turnover time scale (taken to be a constant 300 s for shallow convection) and η is a free parameter of $O(1)$. From (4), $\eta = \varepsilon\tau w_c$, and so it is also possible to use the WRF simulations to test whether a single value of η applies to convection of different depths. The left panel of Fig. 12 shows that this parameterization applied to the CONTROL simulation is not as successful: Not only does η vary with height, but it exhibits different profiles for different depths of convection. The results are somewhat better for FINE but considerably worse for RH90 (not shown). Thus, it cannot be used directly as a universal entrainment parameterization despite its success for shallow cumulus.

Comparing (3) and (4), however, we can see that the Gregory and Neggers et al. schemes are equivalent if we relax the assumption of constant eddy turnover time and instead take $\tau = Aw_c/B$, where $A = \eta/C$. The resulting implied turnover time scale (for $A = 1$) is shown in the right panel of Fig. 12 for the CONTROL and FINE runs. It is greater than 300 s near cloud base and generally less above, and the time scale increases with convection depth. In fact, Fig. 4 of Neggers et al. (2002) actually suggests that τ increases somewhat with convection depth.

Finally, Bechtold et al. (2008) directly parameterize entrainment rate in terms of tropospheric humidity and subsaturation according to

$$\varepsilon(z) = c_0\left(\frac{q_s}{q_{sb}}\right)^2 + c_1\frac{q_s - q}{q}\left(\frac{q_s}{q_{sb}}\right)^3, \tag{5}$$

where q, q_s, and q_{sb} are the environmental specific humidity, the saturation specific humidity at the parcel level, and the saturation specific humidity at cloud base, respectively, and c_0 and c_1 are free parameters of $O(10^{-1})$ if ε is in units of km^{-1}. The first term represents turbulent entrainment and the second term organized entrainment that is applied only to deep convection. This parameterization does not lend itself to a simple scaling test, but we can at least apply the WRF humidity and temperature profiles to determine the implied entrainment rate profile. Figure 13 shows the results for $c_0 = 0.5$ and $c_1 = 0.1$, chosen to give the largest (smallest) possible entrainment rates for shallow (deep) convection. This scheme produces a vertical structure unlike that inferred from the WRF simulations, with entrainment rates becoming very small in the midtroposphere despite the subsaturated relative humidity there and with entrainment rate increasing rather than decreasing with convection depth. The analogous plots for the RH90 simulation (not shown) are very similar. Increasing c_1 makes

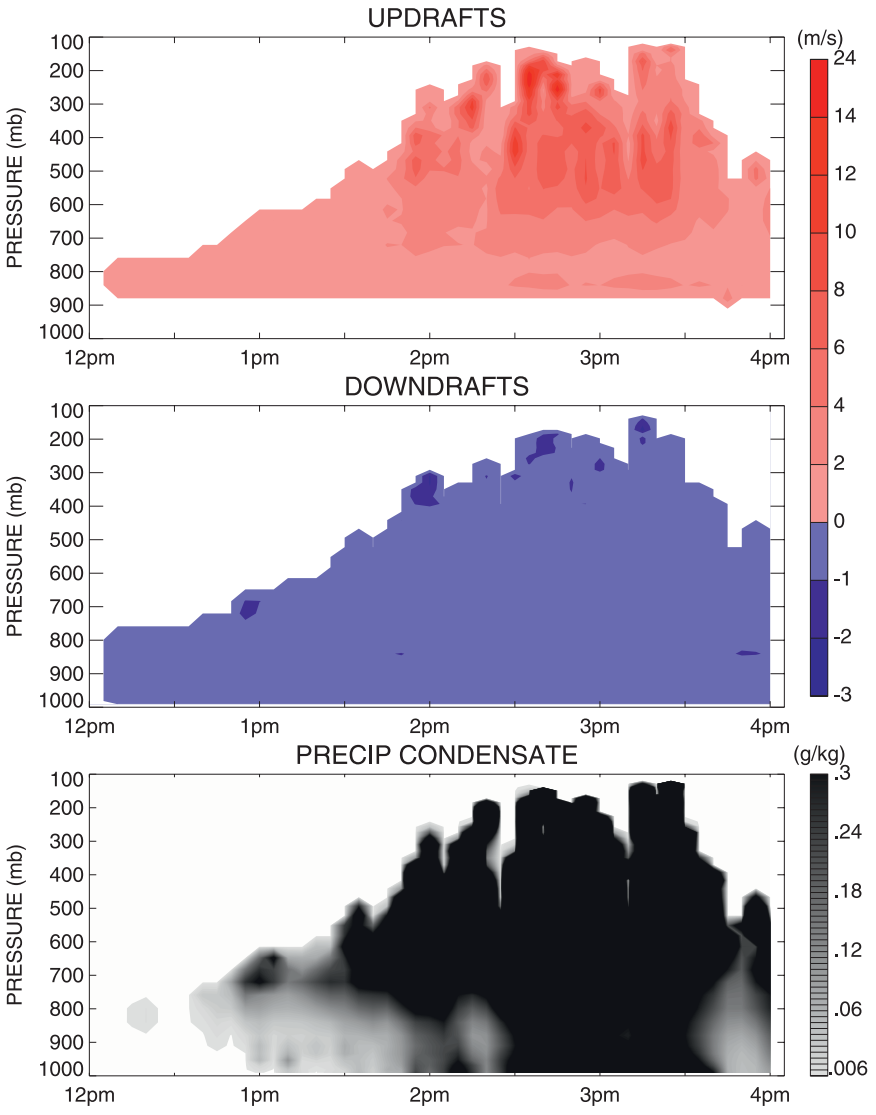

FIG. 10. As in Fig. 3, but for the RH90 simulation.

ε larger at high levels but at the expense of making deep entrainment even greater relative to shallow entrainment, further degrading the comparison with WRF.

5. Role of downdraft cold pools

Although entrainment rate decreases as convection deepens in the WRF simulations, we have not yet established the physical mechanism by which this occurs. Kuang and Bretherton (2006) and Khairoutdinov and Randall (2006) have suggested that the boundary layer cold pools that form after convective downdrafts are initiated are the key to the transition. Cold pool outflow in their simulations creates convergence at the gust front that is organized on a larger spatial scale than other boundary layer turbulence. Invoking classical entraining plume theory in which entrainment varies inversely as plume size, they argue that the larger eddies formed by the cold pool outflow entrain less, allowing previously shallow convective elements to then rise to greater altitudes.

Cold pools are evident in our simulations as well (Fig. 4) and deep convection does first occur soon after the appearance of cold pools, preferentially near their edges. The question is whether parcel size or some other property is the crucial feature that determines their entrainment rate. Figure 14 shows the CONTROL joint distribution of MSE (divided by c_p to express it in temperature units) and vertical velocity near 750 mb (just above the highest cloud base and ~60 mb above mean

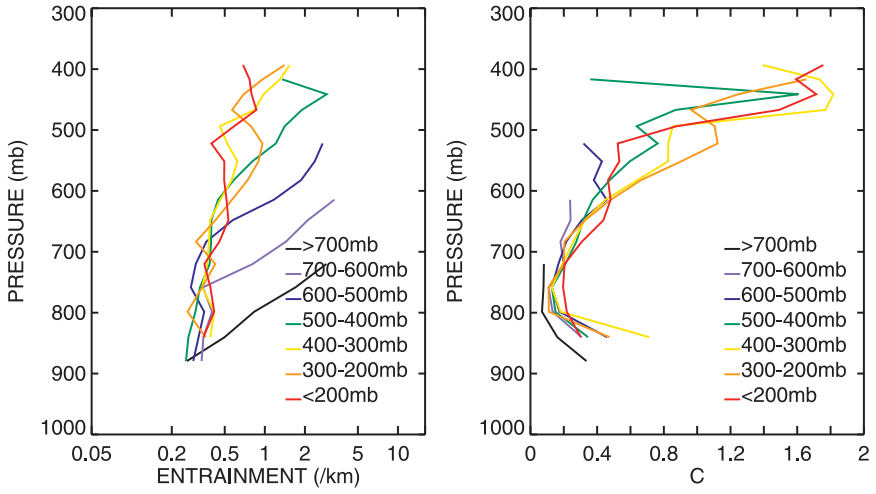

FIG. 11. (left) Entrainment rate and (right) C profiles for the RH90 simulation.

cloud base) for all grid boxes, downdraft grid boxes, and deep convective grid boxes, at different times of day. The mean MSE is ~339 K and its standard deviation is ~2 K over the entire domain (left columns). The mean MSE of deep convective grid boxes is ~8 K higher (right column), consistent with Khairoutdinov and Randall (2006). Downdrafts associated with congestus clouds (middle column) are present at 1400 LT and strengthen from 1430 to 1530 LT. At 1430 LT there is already some evidence of increased updraft speeds in high MSE grid boxes (left column, second row). By the time deep convection develops at 1500 LT, deep convective updraft speeds (right column) are on average about twice that of shallow convective updraft speeds (not shown) near cloud base (~4 versus ~2 m s^{-1}).

The Gregory (2001) parameterization provides a useful framework for understanding how this evolution of conditions leads to weakening entrainment as the afternoon progresses. The high MSE in deep convective cells would by itself imply strong entrainment in the Gregory scheme given its dependence on B. However, the inverse dependence of entrainment on parcel kinetic energy ($1/w_c^2$) in the Gregory parameterization more than offsets this, resulting in weaker entrainment. In other words, rising eddies generated by cold pool convergence spend less time entraining air per unit distance of rise than other turbulent boundary layer eddies and thus entrain less. This view is consistent with the assumption made by Rio et al. (2009) that the transition to deep convection requires sufficient lifting by either

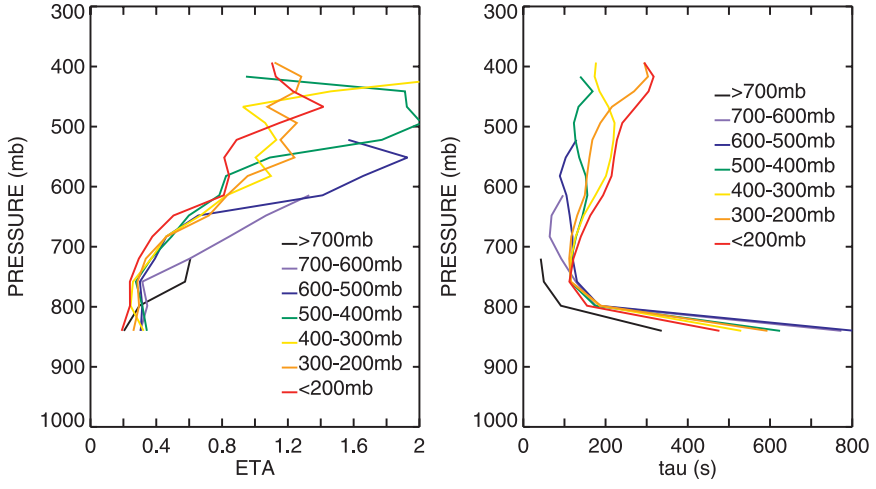

FIG. 12. (left) Mean inferred vertical profiles of the free parameter η in the Neggers et al. (2002) parameterization in CONTROL for convection with tops in various pressure intervals. (right) Mean inferred eddy turnover time τ vertical profiles for convection with tops in various pressure intervals.

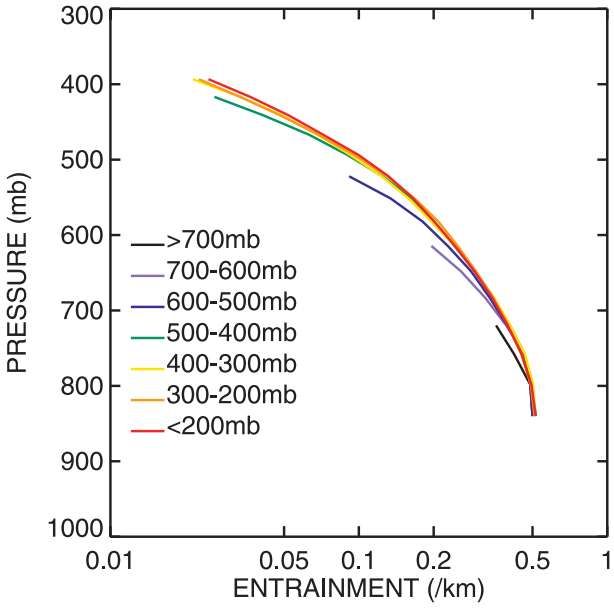

FIG. 13. Entrainment rate profiles in CONTROL for convection with tops in various pressure intervals for the Bechtold et al. (2008) parameterization.

turbulent thermals or at cold pool gust fronts to overcome convective inhibition, but our proposed mechanism is different.

Evidence in the WRF for the alternative view that entrainment weakens as convection deepens because parcel size increases, is mixed. In the context of the Gregory scheme, a larger parcel that entrains less efficiently would use a smaller fraction of its buoyant turbulent kinetic energy generation to accelerate entrained air and thus would have a smaller value of the free parameter C near cloud base. Figure 9 does show some preference for shallower convective types to have somewhat larger cloud base values of C in CONTROL, but this type of behavior is absent in FINE and in RH90 (Fig. 11).

6. Discussion and conclusions

Derbyshire et al. (2004) found that, for identical temperature profiles, CRMs made a transition from shallow to deep convection as free tropospheric relative humidity increased, while SCMs simulated deep convection regardless of the tropospheric humidity. Our simulations are not quite as sensitive to a change in tropospheric humidity—even when we nudge the free troposphere humidity toward 90%, shallow convection exists for several hours, although the transition to deep convection does occur about an hour earlier than in a similar run with drier tropospheric conditions. The difference between our results and those of Derbyshire et al. is most likely the dry continental boundary layer in our simulations (Fig. 1), which prevents rising parcels from gaining access to the more humid air above until sufficient instability builds up in the early afternoon.

Our results suggest that the CRM behavior shown by Derbyshire et al. (2004) is probably not caused by an inherent dependence of entrainment rate on relative humidity, but rather that a sufficiently strong entrainment rate determined by the properties of the buoyant rising parcel will produce the desired sensitivity of convection depth to tropospheric humidity in a GCM. The Gregory (2001) parameterization, which assumes entrainment rate to be directly proportional to parcel buoyancy and inversely proportional to the parcel kinetic energy, appears to have these properties when compared to our WRF simulations for different resolutions and different humidity profiles. The potential advantage of using this scheme, beyond making entrainment rate an interactive parameter that can respond to environmental variations, is that in principle it would allow both shallow and deep convection to be treated with a single unified parameterization that also handles the intermediate congestus stage. The Neggers et al. (2002) approach proposed for shallow convection might also be applied to congestus and deep convection, but only if one relaxes the assumption of a constant eddy turnover time. A buoyancy-based definition of this time scale makes this scheme formally identical to the Gregory (2001) scheme.

In order for the Gregory (2001) parameterization to be implemented in a GCM, it is necessary to specify the vertical profile of its free parameter C as inferred from the WRF simulations in Fig. 9. Gregory assumed constant (but different) values of C for shallow and deep convection in his SCM tests. However, by analogy with the scaling analysis of Grant and Brown (1999), he suggested that C might vary with height as a function of the parcel dilution and the height variation of the updraft speed and mass flux. This requires further study, but we note that the C profile is very similar in the CONTROL and RH90 simulations (Figs. 9, 11), suggesting that the extent of dilution by drier air plays a minor role.

The increase in C with height implied by our simulations appears to be an important feature for GCM parameterizations to capture. For example, J. Wu et al. (2009) found that break period deep convective updraft speed profiles in an SCM with the Gregory (2001) entrainment parameterization and constant C were reasonable up to ~300 mb but became unrealistically strong at higher levels. Gregory deals with this weakness by including an extra drag term in his vertical velocity Eq. (2) proportional to the detrainment rate, which is intended to represent the effects of cumulus-scale pressure gradients. It is unrealistic, however, for such a parameterization to have much effect at levels where the updraft is

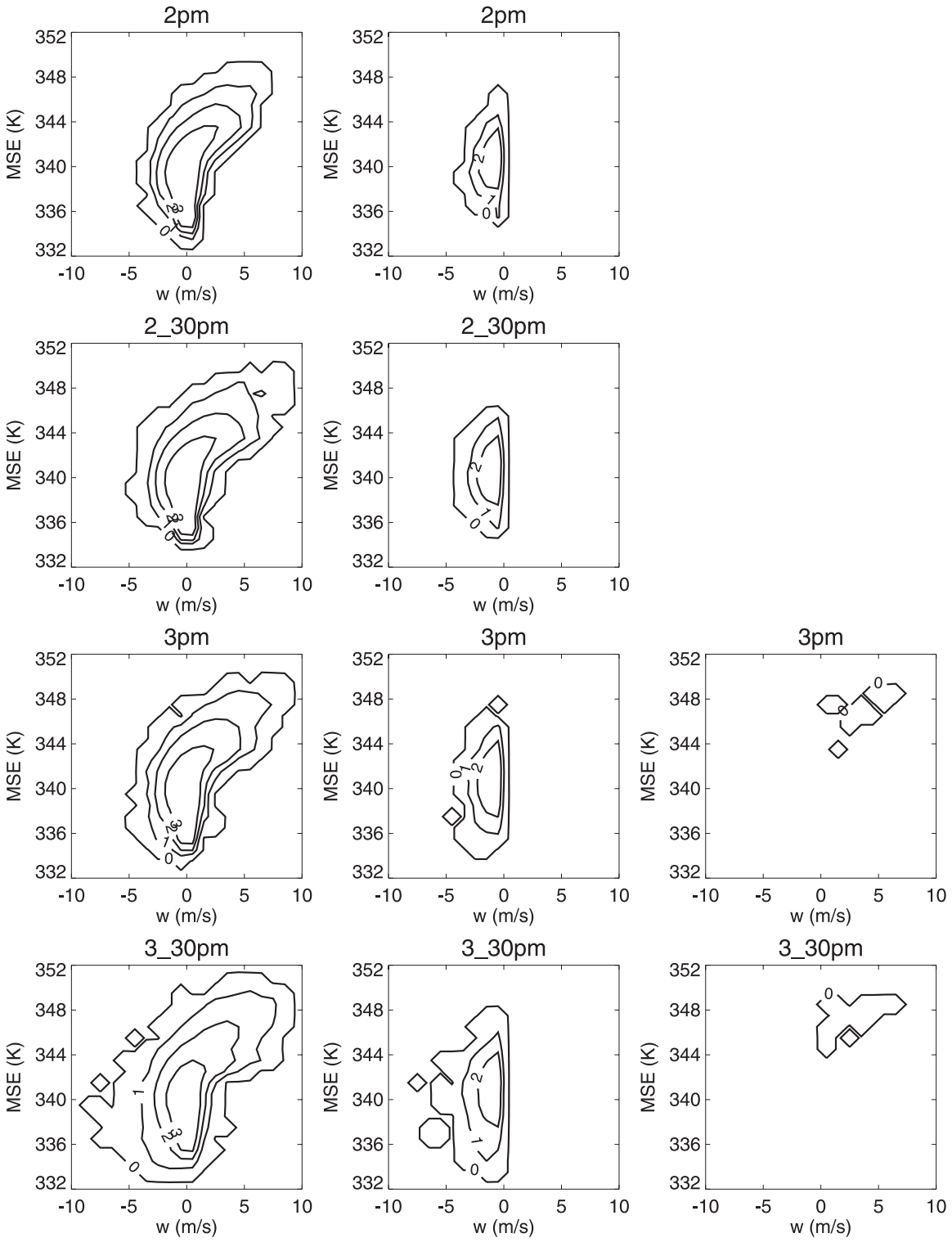

FIG. 14. Joint histograms of ~750-mb frozen moist static energy and vertical velocity at (top) 1400 LT, (second row) 1430 LT, (third row) 1500 LT, and (bottom) 1530 LT for (left) all grid boxes, (center) downdraft grid boxes, and (right) deep convective grid boxes. Deep convection does not exist at 1400 and 1430 LT. Contours are number of occurrences in logarithmic units.

still accelerating, since downward pressure gradient forces tend to occur where the updraft speed converges. A parameterization in which C increases with increasing altitude will eventually terminate the acceleration of the parcel and allow a parameterization of unresolved dynamical effects to decelerate the parcel beyond that.

The surprisingly large entrainment rates we infer in the mid- and upper troposphere may be unique to continental convection. Oceanic convection, which is less buoyant and thus perhaps less turbulent, might therefore have smaller values of C at high altitudes, possibly implying weaker entrainment rates there. For example, Kuang and Bretherton (2006), who also infer entrainment from a CRM, find mean upper-level entrainment rates of $\sim 0.3\ \mathrm{km}^{-1}$ in a maritime case study.

Our results also suggest that implementation of the Gregory (2001) parameterization requires a specification of the initial convective parcel updraft speed enhancement due to downdraft cold pool convergence. Since most cumulus parameterizations now have downdraft parameterizations, this might be represented as a simple function of the downdraft mass flux. A more sophisticated approach would represent the characteristics of the cold pool outflow, which may persist for a time after the downdraft terminates. Another implication of Fig. 14 is that for parameterized GCM deep convective events to reach realistic cloud-top heights in the presence of stronger entrainment than they currently use, the initial parcel properties must be based on MSE values much greater than the gridbox mean.

Our simulations are consistent with previous studies that concluded that CRM-simulated deep convection is sensitive to spatial resolution down to very small scales (approximately 100–200 m). Our simulations are a tradeoff between coarser resolution with a sufficiently large domain size to accumulate reasonable statistics of deep convection (CONTROL) and finer resolution with a smaller domain size in which sampling becomes an issue (FINE). This makes the representation of continental deep convection, which is sparse rather than spatially ubiquitous, a considerable computational challenge. Fortunately, though, the basic behavior of the entrainment process seems to be similar at both resolutions, even though the more turbulent nature of the FINE simulation leads to larger magnitudes of the entrainment rate.

Finally, although we have focused on entrainment in the context of the continental diurnal cycle, it may be equally important to other aspects of convective variability. For example, the transition from the suppressed to the disturbed phase of the Madden–Julian oscillation (MJO) involves a gradual transition from predominantly shallow and congestus convection to more prevalent deep convection (Chen and Del Genio 2009) over a period of days. It has been proposed that preconditioning of tropospheric moisture by prior shallow and midlevel convective events may allow subsequent events to penetrate deeper and thus trigger the disturbed phase (see, e.g., Benedict and Randall 2007). Sufficient sensitivity of a cumulus parameterization to tropospheric humidity may therefore play a role in capturing MJO variability. In addition, Sanderson et al. (2008) find that entrainment is a dominant process regulating global climate sensitivity in a large ensemble of perturbed physics simulations, because it affects the altitude at which convection detrains water vapor and condensate into the environment. Our results indicate that simple constant or inverse-z prescriptions of entrainment, which cannot respond to a climate change, do not capture the relevant physics. Until interactive entrainment schemes are included in GCMs, therefore, one must consider the convective contribution to climate sensitivity to be unconstrained.

Acknowledgments. This research was supported by the Department of Energy Atmospheric System Research Program and by the NASA Precipitation Science Program. We thank three reviewers for constructive comments that improved the manuscript.

REFERENCES

Bechtold, P., M. Köhler, T. Jung, F. Doblas-Reyes, M. Leutbecher, M. J. Rodwell, F. Vitart, and G. Balsamo, 2008: Advances in simulating atmospheric variability with the ECMWF model: From synoptic to decadal time-scales. *Quart. J. Roy. Meteor. Soc.,* **134,** 1337–1351.

Benedict, J. J., and D. A. Randall, 2007: Observed characteristics of the MJO relative to maximum rainfall. *J. Atmos. Sci.,* **64,** 2332–2354.

Betts, A. K., and C. Jakob, 2002: Evaluation of the diurnal cycle of precipitation, surface thermodynamics, and surface fluxes in the ECMWF model using LBA data. *J. Geophys. Res.,* **107,** 8045, doi:10.1029/2001JD000427.

Bryan, G. H., J. C. Wyngaard, and J. M. Fritsch, 2003: Resolution requirements for the simulation of deep convection. *Mon. Wea. Rev.,* **131,** 2394–2416.

Chen, Y., and A. D. Del Genio, 2009: Evaluation of tropical cloud regimes in observations and a general circulation model. *Climate Dyn.,* **32,** 355–369.

Chikira, M., 2008: Development of a cumulus parameterization with environment-dependent lateral entrainment rate. Abstracts, *Fourth Pan-GCSS Meeting, Advances in Modeling and Observing Clouds and Convection,* Toulouse, France, World Climate Research Program, 25.

Dai, A., 2006: Precipitation characteristics in eighteen coupled climate models. *J. Climate,* **19,** 4605–4630.

Derbyshire, S. H., I. Beau, P. Bechtold, J. Y. Grandpeix, J. M. Piriou, J. L. Redelsperger, and P. Soares, 2004: Sensitivity of moist convection to environmental humidity. *Quart. J. Roy. Meteor. Soc.,* **130,** 3055–3079.

Dudhia, J., 1989: Numerical study of convection observed during the winter monsoon experiment using a mesoscale two-dimensional model. *J. Atmos. Sci.,* **46,** 3077–3107.

Grabowski, W. W., and Coauthors, 2006: Daytime convective development over land: A model intercomparison based on LBA observations. *Quart. J. Roy. Meteor. Soc.,* **132,** 317–344.

Grant, A. L. M., and A. R. Brown, 1999: A similarity hypothesis for shallow-cumulus transports. *Quart. J. Roy. Meteor. Soc.,* **125,** 1913–1936.

Gregory, D., 2001: Estimation of entrainment rate in simple models of convective clouds. *Quart. J. Roy. Meteor. Soc.,* **127,** 53–72.

Guichard, F., and Coauthors, 2004: Modelling the diurnal cycle of deep precipitating convection over land with cloud-resolving models and single-column models. *Quart. J. Roy. Meteor. Soc.,* **130,** 3139–3172.

Hirose, M., R. Oki, S. Shimizu, M. Kachi, and T. Higashiuwatoko, 2008: Finescale diurnal rainfall statistics refined from eight years of TRMM PR data. *J. Appl. Meteor. Climatol.,* **47,** 544–561.

Hong, S.-Y., and H.-L. Pan, 1996: Nonlocal boundary layer vertical diffusion in a medium-range forecast model. *Mon. Wea. Rev.,* **124,** 2322–2339.

Jakob, C., and A. P. Siebesma, 2003: A new subcloud model for mass-flux convection schemes: Influence on triggering, updraft properties, and model climate. *Mon. Wea. Rev.,* **131,** 2765–2778.

Janowiak, J. E., V. J. Dagostaro, V. E. Kousky, and R. J. Joyce, 2007: An examination of precipitation in observations and model forecasts during NAME. *J. Climate,* **20,** 1680–1692.

Khairoutdinov, M., and D. Randall, 2006: High-resolution simulation of shallow-to-deep convection transition over land. *J. Atmos. Sci.,* **63,** 3421–3436.

Kuang, Z., and C. S. Bretherton, 2006: A mass-flux scheme view of a high-resolution simulation of a transition from shallow to deep cumulus convection. *J. Atmos. Sci.,* **63,** 1895–1909.

Lin, C., and A. Arakawa, 1997: The macroscopic entrainment processes of simulated cumulus ensemble. Part II: Testing the entraining plume model. *J. Atmos. Sci.,* **54,** 1044–1053.

May, P. T., J. H. Mather, G. Vaughan, C. Jakob, G. M. McFarquhar, K. N. Bower, and G. G. Mace, 2008: The Tropical Warm Pool International Cloud Experiment. *Bull. Amer. Meteor. Soc.,* **89,** 629–645.

Mlawer, E. J., S. J. Taubman, P. D. Brown, M. J. Iacono, and S. A. Clough, 1997: Radiative transfer for inhomogeneous atmosphere: RRTM, a validated correlated-*k* model for the longwave. *J. Geophys. Res.,* **102** (D14), 16 663–16 682.

Neggers, R. A. J., A. P. Siebesma, and H. J. J. Jonker, 2002: A multiparcel model for shallow cumulus convection. *J. Atmos. Sci.,* **59,** 1655–1668.

Nesbitt, S. W., and E. J. Zipser, 2003: The diurnal cycle of rainfall and convective intensity according to three years of TRMM measurements. *J. Climate,* **16,** 1456–1475.

Petch, J. C., A. R. Brown, and M. E. B. Gray, 2002: The impact of horizontal resolution on the simulations of convective development over land. *Quart. J. Roy. Meteor. Soc.,* **128,** 2031–2044.

Rauniyar, S., and K. Walsh, 2009: Diagnosing the effect of the MJO on the diurnal cycle of rainfall in the Southern Hemisphere. *Extended Abstracts, Ninth Int. Conf. on Southern Hemisphere Meteorology and Oceanography,* Melbourne, Australia, Australian Meteorological and Oceanographic Society.

Redelsperger, J.-L., D. B. Parsons, and F. Guichard, 2002: Recovery processes and factors limiting cloud-top height following the arrival of a dry intrusion observed during TOGA COARE. *J. Atmos. Sci.,* **59,** 2438–2457.

Rio, C., F. Hourdin, J.-Y. Grandpeix, and J.-P. Lafore, 2009: Shifting the diurnal cycle of parameterized deep convection over land. *Geophys. Res. Lett.,* **36,** L07809, doi:10.1029/2008GL036779.

Sanderson, B. M., C. Piani, W. J. Ingram, D. A. Stone, and M. R. Allen, 2008: Towards constraining climate sensitivity by linear analysis of feedback patterns in thousands of perturbed-physics GCM simulations. *Climate Dyn.,* **30,** 175–190.

Siebesma, A. P., and J. W. M. Cuijpers, 1995: Evaluation of parametric assumptions for shallow cumulus convection. *J. Atmos. Sci.,* **52,** 650–666.

Simpson, J., and V. Wiggert, 1969: Models of precipitating cumulus towers. *Mon. Wea. Rev.,* **97,** 471–489.

Skamarock, W. C., J. B. Klemp, J. Dudhia, D. O. Gill, D. M. Barker, W. Wang, and J. G. Powers, 2007: A description of the advanced research WRF version 2. NCAR Tech. Note NCAR/TN-468+STR, 88 pp.

Thompson, G., R. M. Rasmussen, and K. Manning, 2004: Explicit forecasts of winter precipitation using an improved bulk microphysics scheme. Part I: Description and sensitivity analysis. *Mon. Wea. Rev.,* **132,** 519–542.

Tokioka, T., K. Yamazaki, A. Kitoh, and T. Ose, 1988: The equatorial 30-60 day oscillation and the Arakawa-Schubert penetrative cumulus parameterization. *J. Meteor. Soc. Japan,* **66,** 883–900.

Wallace, J. M., 1975: Diurnal variations in precipitation and thunderstorm frequency over the conterminous United States. *Mon. Wea. Rev.,* **103,** 406–419.

Wu, C.-M., B. Stevens, and A. Arakawa, 2009: What controls the transition from shallow to deep convection? *J. Atmos. Sci.,* **66,** 1793–1806.

Wu, J., A. D. Del Genio, M.-S. Yao, and A. B. Wolf, 2009: WRF and GISS SCM simulations of convective updraft properties during TWP-ICE. *J. Geophys. Res.,* **114,** D04206, doi:10.1029/2008JD010851.

Xie, S., T. Hume, C. Jakob, S. A. Klein, R. McCoy, and M. Zhang, 2010: Observed large-scale structures and diabatic heating and drying profiles during TWP-ICE. *J. Climate,* **23,** 57–79.

Yang, S., and E. A. Smith, 2006: Mechanisms for diurnal variability of global tropical rainfall observed from TRMM. *J. Climate,* **19,** 5190–5226.

Zhang, G. J., 2009: Effects of entrainment on convective available potential energy and closure assumptions in convection parameterization. *J. Geophys. Res.,* **114,** D07109, doi:10.1029/2008JD010976.